Dalton Transactions

ROYAL SOCIETY OF CHEMISTRY

PAPER

View Article Online
View Journal | View Issue

Cite this: *Dalton Trans.*, 2025, **54**, 5546

Enhancing visible-light-driven photocatalysis of Pd- and Pt-doped WO_3 nanoparticles: the role of oxygen vacancies and bandgap narrowing†

Hyeri Jeon,‡[a,b] Dung Thanh Hoang,‡[c] Hyejin Yu,‡[d] Sunyoung Hwang,[c] Hyun Sung Kim, *[d] Seungwoo Hong *[a,b] and Hangil Lee *[c]

Received 25th December 2024,
Accepted 27th February 2025

DOI: 10.1039/d4dt03540b

rsc.li/dalton

The global energy demand has driven the development of efficient and cost-effective visible-light-activated photocatalysts for the synthesis of fine chemicals. However, most high-performance photocatalysts possess bandgaps exceeding ~3.0 eV, limiting their photocatalytic efficiency under visible light. In this study, Pd- and Pt-doped WO_3 nanoparticles were synthesized. Doping induced oxygen vacancies, which act as electron traps, reducing the bandgap and enhancing visible-light-driven photocatalytic activity. The photocatalytic performance was examined using hydroxymethylfurfural and benzyl alcohol as model substrates. The product yields for both substrates in the presence of Pd-doped WO_3 nanoparticles exceeded 95%. This work demonstrates a simple strategy for enhancing the solar-energy-driven photocatalytic efficiency of metal oxide nanoparticles, promoting sustainable fine chemical synthesis.

Introduction

Owing to increasing energy demands and depleting fossil fuel reserves, researchers are focusing on harnessing solar energy through photocatalysis. Solar energy is a renewable, clean, and inexhaustible resource.[1,2] Consequently, solar-energy-driven photocatalysis is a sustainable, green method. Recent research on photocatalysis has focused on converting a wide range of molecules into valuable chemicals. Metal oxide nanoparticles (MO NPs) exhibit excellent photocatalytic activity and stability and are relatively inexpensive; however, their bandgap (>3.0 eV) significantly limits their visible-light-driven photocatalytic potential.[3,4]

During a photocatalytic NP reaction, the photocatalyst absorbs a photon and reaches a high-energy excited state. The absorbed energy enables electron (e_{CB}^-) transfer from the valence band to the conduction band, leaving holes (h_{VB}^+) in the valence band.[5] These h_{VB}^+ can (i) selectively oxidize useful molecules such as hydroxymethylfurfural (HMF) and benzyl alcohol (BA) and (ii) generate highly reactive hydroxyl radicals ($HO^\bullet$) in an aqueous solution. Similarly, e_{CB}^- can react with O_2 to produce superoxides ($HOO^{\bullet-}$), which are converted into H_2O_2 in an aqueous solution and ultimately generate $HO^\bullet$.[6] HMF conversion and BA oxidation have significant environmental, energy-related, and industrial implications. The conversion of HMF, a key biomass-derived platform chemical, into valuable biofuels, fine chemicals, and polymers is a sustainable solution for mitigating climate change by promoting a circular economy. The oxidation of BA to benzaldehyde and other fine chemicals is a common step during the production of fragrances, flavors, and active pharmaceutical ingredients in the cosmetics, food, and pharmaceutical industries, respectively. The photocatalytic conversion of HMF and BA addresses urgent environmental and industrial requirements and promotes greener, more sustainable chemical processes.

Among the various MO NPs, n-type semiconductor photocatalysts, such as tungsten oxide (WO_3) NPs, have garnered tremendous attention over the past few decades owing to their advantageous physicochemical properties, including low cost, chemical inertness, and high exciton binding energy (~60 MeV).[7–10] Pure WO_3 NPs exhibit a bandgap of ~3.3 eV, which achieves a limited light response and absorption efficiency in the visible spectrum; therefore, we must develop strategies for optimizing their visible-light-driven photocatalysis. Doping WO_3 NPs with precious metal ions such as Pd and Pt would optimize their bandgaps for visible-light-driven photocatalysis. Moreover, doping creates abundant oxygen vacancies (V_Os) on the WO_3 NP surfaces, which produce additional electronic

[a]*Department of Chemistry & Nanoscience, Ewha Womans University, Seoul, 03760, Republic of Korea*
[b]*Graduate Program in Innovative Biomaterials Convergence, Ewha Womans University, Seoul 03760, Korea*
[c]*Department of Chemistry, Sookmyung Women's University, Seoul 04310, Republic of Korea*
[d]*Department of Chemistry, Pukyong National University, Busan 48513, Republic of Korea*

†Electronic supplementary information (ESI) available: STEM-EDS, BET analysis, enlarged XRD pattern, LC-MS, reaction pathway, kinetics, recycle experiments. See DOI: https://doi.org/10.1039/d4dt03540b

‡These authors contributed equally to this work.

charge carriers and promote the oxidation of molecules on the surface.[11,12]

In this study, we doped WO_3 NPs with Pd and Pt (Pd@WO_3 and Pt@WO_3) and analyzed their morphology, chemical bonding structure, and electronic structure *via* high-resolution transmission electron microscopy (HRTEM), powder X-ray diffraction (PXRD), Raman spectroscopy, and X-ray photoelectron spectroscopy (XPS). Subsequently, we assessed their visible-light-driven photocatalytic performance during the oxidation of HMF and BA.[13]

Experimental

Preparation of WO_3 and NM@WO_3 NPs

To synthesize pristine WO_3 NPs, two precursor solutions, sodium tungstate dihydrate ($Na_2WO_4{\cdot}2H_2O$; 3.0 g) and HCl (0.1 M) in 100 mL of distilled deionized water (DDW), were prepared separately and gradually mixed with gentle stirring for 1 h until a yellow precursor was obtained.[14]

The mixed solution was then placed in an autoclave at 220 °C for 10 h. The produced WO_3 NPs were filtered and washed twice with DDW to remove any residues and dried at 90 °C for 48 h. After synthesizing the pristine WO_3 NPs, we obtained Pd@WO_3 and Pt@WO_3 NPs through the following procedure. The desired amounts of each noble metal ion source (5 mol% of $PdCl_2$ and $PtCl_2$) were added to the synthesized WO_3 NPs (1.0 g) and stirred continuously for 3 hours at 90 °C. The mixed solution was transferred to autoclaves and heated at 220 °C for 10 h in a convection oven. The produced NM@WO_3 NPs were filtered and washed five times with DDW to remove any residues and dried at 90 °C for 48 h. They were then washed 10 times with DDW and five times with ethanol, followed by drying at 95 °C. After synthesis, each sample was subjected to quantitative analysis of Pd and Pt using X-ray fluorescence (XRF), and the results indicated values close to the intended amounts, measuring 5.3% and 5.1%, respectively.

Characterization

The morphologies of the samples were observed using a JEM-ARM200F (JEM-ARM200F (NEOARM), JEOL Ltd, Japan) equipped with an energy-dispersive X-ray spectrometer. X-ray diffraction (XRD) patterns for pristine WO_3, Pd@WO_3, and Pt@WO_3 NPs were acquired using a D8 Advance TRIO/TWIN diffractometer (Bruker, USA) with Ni-filtered Cu Kα radiation at Sookmyung Women's University and a D/MAX-2200/VPC Rigaku at the National Research Facilities and Equipment Center (NanoBio·Energy Materials Center) at Ewha Womans University. Quantitative analysis of Pd and Pt on WO_3 was performed using an X-ray fluorescence spectrometer (Rigaku/ZSX-Primus IV) (Table S1†). Raman spectra were acquired by using a custom-made setup and were calibrated using the Si peak (520.89 cm^{-1}) as an internal reference. The light source used was a 532 nm laser with 1.02 mW power. Ultraviolet–visible diffuse reflectance spectroscopy (UV-Vis DRS) measurements were performed using a Shimadzu UV-2600i UV-Vis spectrophotometer equipped with integrating spheres. The nitrogen adsorption isotherms of the samples were collected at 77 K using a BELsorp-Max system (BEL) to measure the surface area of the three tested WO_3 NPs. To detect the presence of V_Os on the surface of the WO_3 NPs, electron paramagnetic resonance (EPR; JES-X320, JEOL Ltd) spectra, ranging from 300 to 400 mT, were obtained at 300 K at a frequency of 9446 MHz, a power of 10 mW, a modulation frequency of 100 kHz, and a width of 0.4 mT. To compare the electronic structures of the three tested samples, we performed XPS and work-function analysis at the 8A1 beamline in the Pohang Accelerator Laboratory. The W 4f, Pt 4f, Pd 3d, and O 1s core-level spectra were obtained using photon energies of 150, 200, 450, and 600 eV, respectively. The binding energies of the core-level electrons were compared to that of the clean Au 4f core level at the same photon energy.

Photocatalytic measurement

The photocatalytic conversion activities of WO_3, Pd@WO_3 and Pt@WO_3 NPs were determined using the oxidation of 25 mM 2,5-hydroxymethylfurfural (HMF, Sigma-Aldrich, 99%, 0.315 g) and 25 mM benzyl alcohol (BA Sigma-Aldrich, 99%, 0.270 g) in 100 mL of DDW.[15] No uncommon hazards are noted. The prepared pristine WO_3 and the two modified WO_3 NPs (0.015 g) were dispersed in distilled water (30 mL) under sonication. This aqueous suspension was stirred for 2 h to allow the equilibrium adsorption of HMF and BA on the three WO_3 NPs. A 300 W Xe arc lamp (Oriel) equipped with a 10 cm IR water filter and a cutoff filter (λ > 420 nm) was used as the light source. The photocatalytic conversion activities of HMF and BA were analyzed using high-performance liquid chromatography (HPLC-20AD pump, Shimadzu). The oxidation products of HMF and BA were analyzed *via* a HPLC-MS (ULTIMATE 3000 RSLC SYSTEM (Thermo) and Q-EXACTIVE ORBITRAP PLUS MS (Thermo)).

Results and discussion

The HRTEM images in Fig. 1 show the phase distributions and crystal structures of the three WO_3 NPs. The corresponding fast Fourier transform (FFT) and line profiles were simultaneously obtained at the atomic scale (inset of Fig. 1). Fig. 1a displays a low-magnification TEM image of the WO_3 NPs (yellow box). The corresponding FFT pattern indicates a single-crystal structure. The TEM image confirms a clear lattice fringe of 0.372 nm, which is consistent with the interplanar spacing of the (020) plane of WO_3. This indicates a highly crystalline hexagonal WO_3 phase (Fig. 1a).[16,17]

The interatomic distances on the surfaces of Pd@WO_3 and Pt@WO_3 NPs were determined from their FFT patterns (Fig. 1b and c, respectively).[18] Pd and Pt ions were observed in the crystalline structures on the WO_3 NP surfaces. The HRTEM image of Pd@WO_3 NPs (Fig. 1b, yellow box) shows two distinct lattice fringes, corresponding to the WO_3 NPs and crystallized PdO on the WO_3 NP surfaces. The (002) lattice fringe spacing

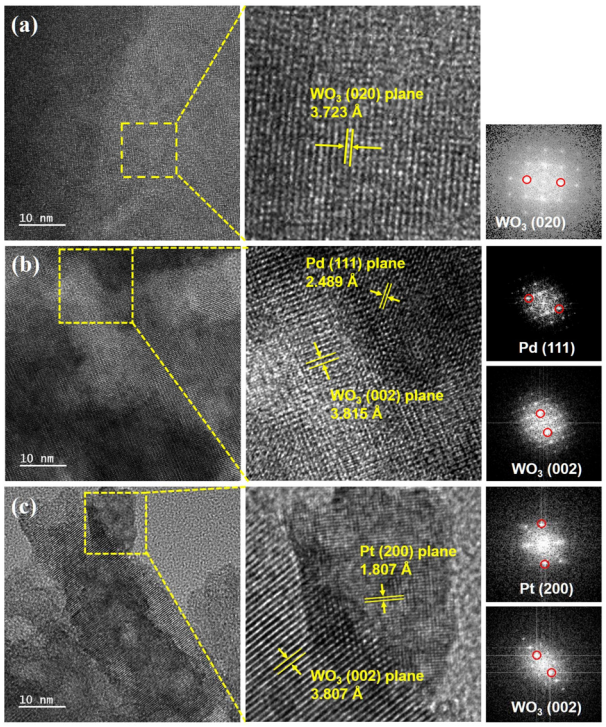

Fig. 1 High-resolution transmission electron microscopy images and the corresponding fast Fourier transform images of (a) WO_3, (b) 5 wt% Pd@WO_3, and (c) 5 wt% Pt@WO_3 nanoparticles (NPs).

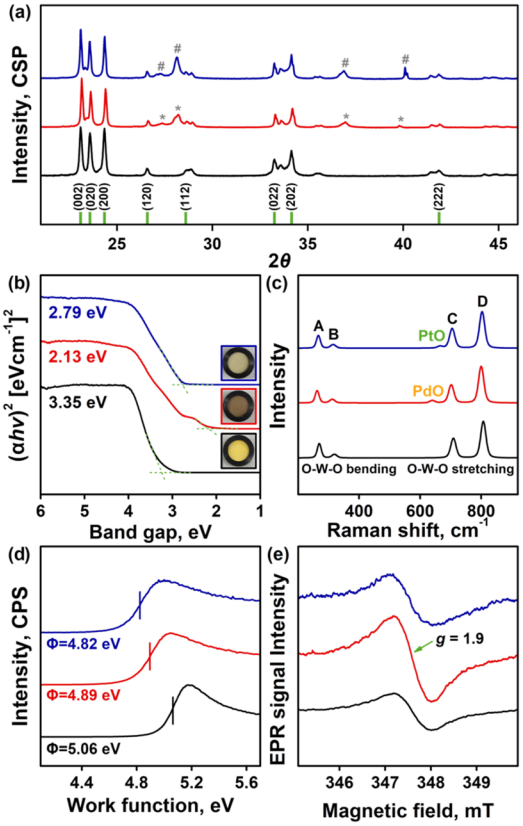

Fig. 2 (a) PXRD, (b) UV-Vis DRS spectra, (c) Raman spectra, (d) work function (ϕ) measurements, and (e) EPR data of pristine WO_3 (black), Pd@WO_3 (red), and Pt@WO_3 (navy blue).

of WO_3 was 0.382 nm, which is consistent with that of pristine WO_3 NPs. The (111) lattice fringe spacing of Pd was 0.249 nm, which is larger than the (111) interplanar distance in the face-centered cubic (fcc) Pd structure (0.225 nm). This indicates that the Pd ions were successfully doped into WO_3 in the form of PdO.[19] Similarly, the HRTEM image of Pt@WO_3 NPs shows two lattice fringes (Fig. 1c). The (002) lattice fringe spacing of WO_3 was identical (0.381 nm) to that of the pristine WO_3 NPs. The Pt (200) lattice fringe spacing was reduced to 0.181 nm, which is smaller than the (200) interplanar distance of the fcc Pt structure (0.19 nm).[20] These findings suggest that Pt@WO_3 and Pd@WO_3 NPs may exhibit different catalytic properties. The elemental distribution of the synthesized NPs was examined using energy-dispersive X-ray spectroscopy. Pd, Pt, W, and O were homogeneously distributed across the NPs (Fig. S1†).

The N_2 adsorption–desorption isotherms of the NPs were acquired to determine their Brunauer–Emmett–Teller (BET) surface areas.[21] The surface areas of WO_3, Pd@WO_3, and Pt@WO_3 NPs were determined to be 26.3, 35.9, and 32.1 $m^2 g^{-1}$, respectively. The doped NPs had higher surface areas (Fig. S2†). This could be attributed to the differences in their ionic radii (W^{6+}, 74 pm; Pt^{2+}, 94 pm; and Pd^{2+}, 100 pm), which likely cause surface defects on the WO_3 NP surfaces upon Pt and Pd doping.

The crystallinity and crystal planes of the three WO_3 NPs were analyzed *via* PXRD (Fig. 2a).[22] All samples exhibited characteristic 2θ peaks at 23.09°, 23.58°, 24.34°, 26.59°, 28.60°, 33.25°, 34.15°, and 41.88°, corresponding to the reflections from the (002), (020), (200), (120), (112), (022), (202), and (222) planes of WO_3, respectively. These prominent reflection patterns clearly indicate good crystallization (JCPDS No. 83-0950).[23] These patterns are consistent with the formation of monoclinic WO_3 (m-WO_3).[24] The lattice parameters of the unit cells of pristine WO_3 were as follows: a = 7.68, b = 7.72, c = 7.75, $\alpha = \gamma = 90°$, and β = 90.77°. However, the unit cells of Pt@WO_3 were slightly larger than those of pristine WO_3 (a = 8.35, b = 7.30, c = 7.85, $\alpha = \gamma = 90°$, and β = 106.1°). In contrast, the unit cells of Pd@WO_3 were slightly smaller than those of pristine WO_3 (a = 7.59, b = 7.53, c = 5.54, $\alpha = \gamma = 90°$, and β = 105.1°).[25] These results suggest that doping did not induce significant phase transitions. The new peaks in the PXRD patterns of Pd@WO_3 (marked *) and Pt@WO_3 (marked #) were attributed to PdO and PtO, respectively. However, the formation of these metal oxides on the WO_3 NP surfaces did not significantly alter the overall structure of WO_3.[26] The high-intensity peaks corresponding to WO_3 in the PXRD patterns of Pd@WO_3 and Pt@WO_3 NPs slightly shifted to larger angles owing to metal doping (Fig. S3†). This also confirms the presence of defects on the WO_3 surface (*i.e.*, a smaller unit cell).

The Scherrer equation (eqn (1)) was used to determine the average crystallite size of the NPs based on the peak with the

highest intensity (~22.9°), corresponding to the [002] reflection.

$$D = 0.9\lambda/B\cos\theta \quad (1)$$

where D is the crystallite size (nm), λ is the wavelength of the X-ray radiation (0.154 nm), θ is Bragg's angle, and B is the full width at half maximum (FWHM) of the 2θ peak. The nanoscale crystallite sizes are summarized in Table S2.† The crystallite sizes of the three NPs were in the range of 60.5–63.2 nm.[27]

The UV-visible diffuse reflectance spectra (UV-vis DRS) of the NPs were analyzed using the Kubelka–Munk function, which is proportional to the absorption coefficient. The bandgap (E_g) was determined using Tauc's plot in combination with the Kubelka–Munk function.[28] The band gap was then estimated using Tauc's equation (eqn (2)), where hn is the photon energy and A is a proportionality constant.

$$(F(R)hn)^2 = A(hn - E_g) \quad (2)$$

A plot of $(F(R)hn)^2$ *versus* hn was constructed, and the linear region was extrapolated to the energy axis to determine the band gap energy as shown in Fig. 2b. The calculated approximate bandgaps for WO_3, Pd@WO_3, and Pt@WO_3 NPs were 3.35, 2.13, and 2.79 eV, respectively.[29]

The vibrational frequencies of the W–O bonds in WO_3, Pd@WO_3, and Pt@WO_3 NPs were obtained through Raman spectroscopy (Fig. 2c). All three samples demonstrated W–O–W–O–W bending modes at 272 and 325 cm^{-1} (denoted as A and B), asymmetric O–W–O vibrations at 718 cm^{-1} (denoted as C), and symmetric O–W–O vibrations at 807 cm^{-1} (denoted as D).[30] These active vibration modes confirm the presence of a single, dominant WO_3 NP phase and are consistent with the XRD results. However, the peak positions of the Pd@WO_3 and Pt@WO_3 NPs downshifted compared to those of the WO_3 NPs.[31] This suggests that Pt and Pd doping lowered the W–O bond stretching energy, which confirms the formation of a defect structure on the surface of the WO_3 NPs.[32]

The charge transfer between WO_3 and the doped Pd and Pt ions in the defect structure was determined *via* work function measurements (Fig. 2d).[33] Doping WO_3 NPs with 5 wt% Pd and Pt ions shifted the secondary electron edge energies from 5.06 eV to 4.89 and 4.82 eV for Pd@WO_3 and Pd@WO_3, respectively. This negative shift in the work function (~0.2 eV) suggests a smoother charge carrier transfer, whether by light or electrons. This indicates the higher photocatalytic potential of the doped WO_3 NPs.[34] Electron paramagnetic resonance (EPR) spectroscopy was performed to confirm the increase in V_Os in the Pd@WO_3 and Pt@WO_3 NPs (Fig. 2e).[35] The EPR signal centered at g = 1.9 was attributed to the Zeeman effect induced by a single electron trapped within the anionic V_Os on the WO_3 NP surfaces. An EPR signal at g = 1.9 was also observed for Pt@WO_3 NPs. The spin quantification calculated by integrating this signal revealed that Pt@WO_3 had 1.3 times the V_Os of the WO_3 NPs.[36] Moreover, the Pd@WO_3 NPs exhibited an EPR signal at g = 1.9. The calculated spin quantification revealed that Pd@WO_3 NPs had 3 times the V_Os of the WO_3 NPs. These results confirm the abundance of V_Os in the Pt@WO_3 and Pd@WO_3 NPs compared to that in the WO_3 NPs.

The bonding configurations of the W and O atoms and the electronic structural changes induced by the doped Pd and Pt on the WO_3 NP surfaces were examined *via* XPS (Fig. 3).[37] The W 4f core-level XPS profile exhibited two W $4f_{7/2}$ peaks at 34.8 and 32.3 eV, corresponding to W^{6+} in WO_3 and W^{x+} in the WO_3 defects (WO_x), respectively (Fig. 3a).[38] The WO_x peak intensity was significantly higher for Pd@WO_3 and Pt@WO_3 NPs, which could be attributed to the abundant V_Os on their surfaces.[39] However, the Pd@WO_3 NPs had a higher number of defects than the Pt@WO_3 NPs. The O 1s core-level XPS profile showed three peaks at 530.5, 531.7, and 532.8 eV, corresponding to WO_3, V_Os, and –OH, respectively (Fig. 3b).[40] The peak intensity at 531.7 eV for Pd@WO_3 NPs was higher than those of Pt@WO_3 and WO_3 NPs. This confirms that the Pd@WO_3 NPs have a higher number of defects and V_Os than Pt@WO_3 NPs. These results suggest that Pd@WO_3 NPs could exhibit the best photocatalytic performance among the three WO_3 NPs.[41] The Pd 3d and Pt 4f core-level XPS profiles are shown in Fig. 3c and d, respectively. The peaks at 73.2 and 77.5 eV in the Pt XPS profile of Pt@WO_3 NPs correspond to Pt^{2+} in PtO, while those at 72.1 and 74.5 eV correspond to PtO_x formed because of V_Os. The peaks at 343.5 and 338.0 eV in the Pd XPS profile of Pd@WO_3 NPs correspond to Pd^{2+} in PdO, while those at 341.5 and 335.5 eV correspond to PdO_x formed because of the V_Os on the WO_3 NP surfaces. The formation of PtO and PdO on the surfaces of the WO_3 NPs reduced the number of O atoms on the WO_3 NP surfaces. However, a higher amount of PdO_x was formed on the Pd@WO_3 NPs than that of PtO_x on the Pt@WO_3 NPs (Fig. 3c and d). This indicates a higher number of V_Os on the Pd@WO_3 NPs than on the Pt@WO_3 NPs.[42] This suggests that the Pd@WO_3 NPs have the narrowest bandgap among the samples and could exhibit the highest photocatalytic performance.[43–45]

Fig. 4 shows the X-ray absorption near-edge structure (XANES) spectra and soft X-ray absorption spectra (XAS) of the

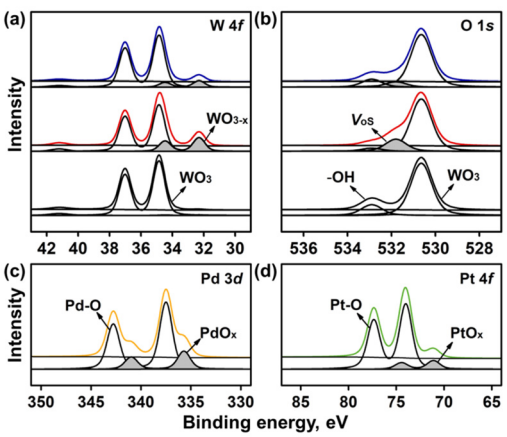

Fig. 3 (a) W 4f and (b) O 1s X-ray photoelectron spectra of WO_3 (black), Pd@WO_3 (red), and Pt@WO_3 NPs (navy blue). (c) Pd 3d and (d) Pt 4f core-level spectra.

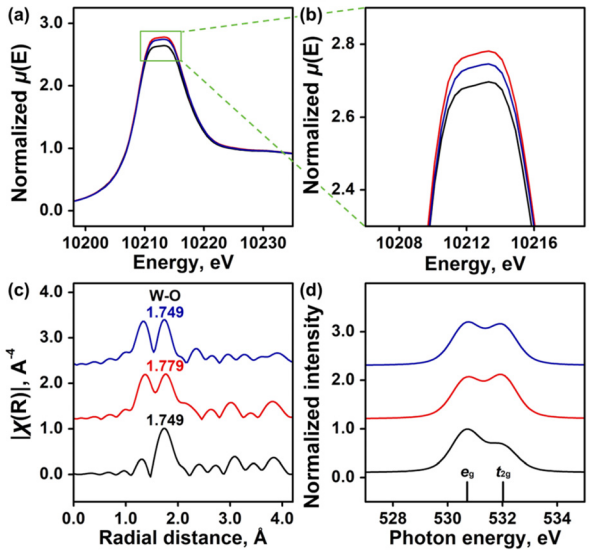

Fig. 4 (a) Overlaid W L_3-edge X-ray absorption near-edge structure (XANES), (b) magnified W L_3-edge XANES, (c) Fourier transform extended X-ray absorption fine structure (EXAFS), and (d) O K-edge spectra of WO_3 (black line), Pd@WO_3 (red), and Pt@WO_3 NPs (navy blue).

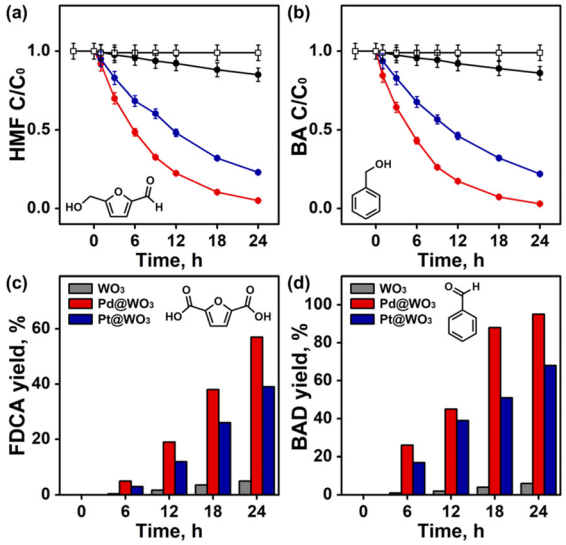

Fig. 5 Photocatalytic conversion activities of pristine WO_3, Pd@WO_3, and Pt@WO_3 NPs during the conversion of (a) hydroxymethylfurfural (HMF) and (b) benzyl alcohol (BA) with and without 5,5-dimethyl-1-pyrroline *N*-oxide (DMPO; gray). Reaction conditions: [catalyst] = 0.5 g L^{-1}, $\lambda \geq 420$ nm, and $[HMF]_0 = [BA]_0 = 25$ mM. Yields of (c) 2,5-furandicarboxylic acid (FDCA) from HMF and (d) benzaldehyde (BAD) from BA with increasing time of 420 nm irradiation.

three WO_3 NPs. W L_3-edge XANES was used to study the electronic transitions from the $2p_{3/2}$ orbitals to the vacant d orbitals of the WO_3 NPs.[46,47] All NPs exhibited a rising edge peak at ~10 212.5 eV, suggesting that the W^{6+} ions in all three NPs are the dominant metal ions (Fig. 4a). However, higher peak intensities were observed for the Pd@WO_3 and Pt@WO_3 NPs, indicating an abundance of V_Os (Fig. 4b). This difference in the intensities suggested that the amount of V_Os increased in the order of WO_3 < Pt@WO_3 < Pd@WO_3 NPs, which was consistent with the spectroscopic results described above. Fig. 4c exhibits the Fourier transform (FT) of the W L_3-edge EXAFS $k^3\chi$ data of the NPs in the range of k = 3–11 $Å^{-1}$.[48] The peak at 1.749–1.779 Å (phase-corrected values) corresponds to the average bond lengths of the W–O coordination shells in the WO_6 octahedron. Very interestingly, W–O bonds within Pt@WO_3 NPs remained identical to those in the pristine WO_3 NPs, while Pd doping noticeably affected the first W–O coordination shell, leading to an increase of 0.03 Å. Fig. 4d shows the O K-edge XAS spectra of the three WO_3 NPs. It was found that the peak intensity originating from the e_g orbital decreased upon doping with Pt^{2+} and Pd^{2+} ions, while the t_{2g} signal intensity significantly increased. This result suggested changes in the electronic structures of the unoccupied states within WO_3 NPs and, thereby, alterations in their defect structures.[49] The increase in t_{2g} signal intensity accompanied by a decrease in e_g signal intensity indicated that the changes in the absorption intensity ratio between e_g and t_{2g} orbitals generated additional defect structures in WO_3 NPs through a mixing of tetrahedral and octahedral geometries.

Fig. 5 shows the photocatalytic conversion efficiencies of HMF and BA in the presence of the three WO_3 NPs under visible-light irradiation and the yields of 2,5-furandicarboxylic acid (FDCA) and benzaldehyde (BAD) from HMF and BA, respectively.[50,51] When the radical scavenger 5,5-dimethyl-1-pyrroline *N*-oxide (DMPO) was used, HMF and BA were not converted into the desired products under visible-light irradiation, indicating that the radical scavenger consumed the generated radical species. Moreover, the WO_3 NPs did not convert HMF or BA, presumably because of their large bandgap. It is also noteworthy that there are no reported cases of HMF and BA conversion using other transition metal ion-doped WO_3 (Table S3†). While some transition metals may exhibit similar defect-engineering properties, Pd and Pt were chosen due to their superior stability and catalytic performance under visible light.

However, the Pd@WO_3 and Pt@WO_3 NPs showed higher photocatalytic degradation (PCD) of HMF and BA under visible-light irradiation compared to the WO_3 NPs. The Pd@WO_3 NPs exhibited the highest PCD efficiency, which is consistent with the XPS and DRS results. This enhanced PCD efficiency is attributed to the extensive defect structures on the Pd@WO_3 NP surfaces. Table 1 summarizes the 24 h PCD profiles of HMF and BA for the three WO_3 NPs under 420 nm irradiation.

The yields of FDCA (Fig. 5c) are consistent with the PCD efficiency of HMF (Fig. 5a). The Pd@WO_3 NPs demonstrated the highest FDCA yield. As the selective oxidation of the –OH or –CHO groups of HMF to produce FDCA is a key photocatalytic conversion reaction, we must identify the functional groups that participate in the oxidation of HMF in the presence of WO_3, Pd@WO_3, and Pt@WO_3 NPs (Fig. S4†). In all three biomass conversion reactions, the –OH group of HMF

Table 1 Photocatalytic degradation (PCD, C/C_0 [a]) efficiencies of HMF and BA and yields of FDCA and BAD for WO_3, Pd@WO_3, and Pt@WO_3 NPs after 24 h of 420 nm irradiation

	WO_3	Pd@WO_3	Pt@WO_3
C/C_0 of HMF	0.85 ± 0.042	0.050 ± 0.003	0.23 ± 0.012
C/C_0 of BA	0.86 ± 0.003	0.030 ± 0.002	0.22 ± 0.011
FDCA (%)	5.0	57	39
BAD (%)	6.0	95	68

[a] C and C_0 are the time-dependent and initial concentrations of HMF and BA.

was selectively oxidized to –CHO, affording 2,5-diformylfuran (DFF) as the sole intermediate, which was further oxidized to FDCA, regardless of the variations in the ratio of the two species (Scheme 1).[52]

We analyzed the liquid chromatography-mass spectrometry profiles of the photocatalytic biomass conversion reactions on the three WO_3 NPs and derived a plausible catalytic mechanism. The V_Os on the WO_3 NP surfaces trap electrons, which react with the O_2 present in air-saturated water, affording $O_2^{\bullet-}$ species. Radical trapping experiments with DMPO confirmed the generation of $O_2^{\bullet-}$ species (gray circles in Fig. 5a and b). These $O_2^{\bullet-}$ species oxidize HMF to DFF and then to FDCA with the assistance of h^+. Both Pd@WO_3 and Pt@WO_3 NPs showed enhanced oxidation efficiencies for the conversion of BA to BAD (Fig. 5d). This is attributed to the higher number of defects on their surfaces.[53] Table 1 summarizes the yields of FDCA and BAD from 25 mM HMF and BA, respectively, over 24 h obtained using the three WO_3 NPs under visible-light irradiation.

We observed a linear correlation between $\ln(C/C_0)$ and the reaction time for the three WO_3 NPs, indicating pseudo-first-order kinetics. The calculated first-order rate constants (k) (Fig. S5†) for the HMF PCD for pristine WO_3, Pd@WO_3, and Pt@WO_3 NPs were 0.0067, 0.13, and 0.061 h^{-1}, respectively. The k values of the BA PCD for pristine WO_3, Pd@WO_3, and Pt@WO_3 NPs were 0.0063, 0.15, and 0.063 h^{-1}, respectively. This indicates that the reaction rates of Pd@WO_3 NPs are over 17 (for PCD of HMF) and 22 (for PCD of BA) times higher than those of the WO_3 NPs. The photocatalytic activity of the three NPs was sustained (>97%) even after ten cycles (Fig. S6†).

The improved photocatalytic activity of WO_3 NPs under visible-light irradiation can be partially attributed to the narrow bandgap of Pd@WO_3 and Pt@WO_3 NPs, along with an increase in V_Os. The Pd@WO_3 NPs exhibited higher reactivity than the Pt@WO_3 NPs in the photocatalytic HMF conversion owing to their higher density of V_Os. In typical photocatalysts, charge carriers are generated near the surface due to exciton formation and subsequent charge separation. Owing to the short carrier diffusion length, surface defects often serve as trap states that enhance the photocatalytic reactivity, depending on the density of V_Os and the associated bandgap changes (Scheme 1).

The different valence states of Pd^{2+} and Pt^{2+} compared to W^{6+} in the host WO_3 facilitate the generation of V_Os through efficient charge transfer,[54] enhancing photocatalytic oxidation.[55] The Shannon effective ionic radii of W^{6+}, Pd^{2+}, and Pt^{2+} were 74 pm, 94 pm, and 100 pm, respectively. This suggests that cation doping, especially with Pd^{2+}, induces lattice strain in the host WO_3 NPs, acts as a reducing agent, and generates atomic defects, altering their electronic structure.[56,57] In addition, the different valence states of the doped cations compared to W^{6+} in the host WO_3 indicate the crucial role of V_Os in the photocatalytic activity of the doped WO_3 NPs. Overall, the Pd@WO_3 NPs showed the highest photocatalytic activity.

Conclusions

WO_3 NPs intrinsically exhibit very weak catalytic activity under visible light. In this study, we successfully engineered WO_3 NPs by doping with Pd and Pt ions. Atomic-scale analysis confirmed the generation of oxygen vacancies V_Os. Despite structural similarity in bulk phases, these defects, induced by local asymmetries in the electron and hole concentrations, lowered the semiconductor bandgap and dramatically enhanced photocatalytic conversion. The Pd@WO_3 and Pt@WO_3 NPs efficiently converted HMF to FDCA and BA to BAD in neutral water as the formal oxidant under visible light. In particular, the Pd@WO_3 NPs exhibited >95% PCD rates for HMF and BA. The yields of FDCA and BAD were 57% and 95%, respectively. This study highlights the crucial role of V_Os and local electronic asymmetries in tuning metal oxide photocatalysts. Future efforts should focus on optimizing the dopant concentration and exploring alternative transition metal dopants to further enhance catalytic efficiency. The development of high-performance, visible-light-driven photocatalysts will advance the utilization of solar energy.

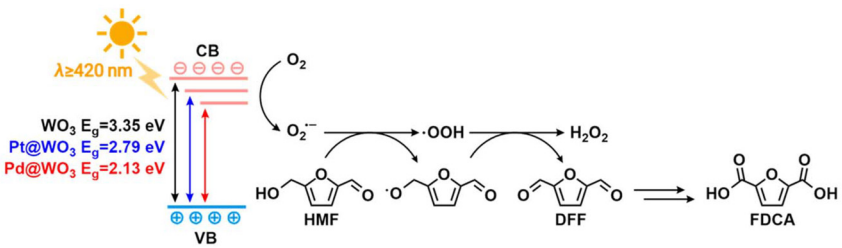

Scheme 1 Illustration of the distinct reaction and charge transport mechanisms in photocatalysis by WO_3, Pd@WO_3, and Pt@WO_3 NPs.

Author contributions

Hyeri Jeon, Dung Thanh Hoang, and Hyejin Yu: formal analysis, investigation, visualization, and writing – review & editing. Hyun Sung Kim, Hangil Lee, and Seungwoo Hong: conceptualization, formal analysis, funding acquisition, project administration, writing – original draft, and writing – review & editing.

Data availability

The data supporting this article have been included as part of the ESI.†

Conflicts of interest

There are no conflicts to declare.

Acknowledgements

This work was supported by the National Research Foundation of Korea (NRF) grants funded by the Korean government (MSIT) (RS-2024-00346153). This work was supported by the National Research Foundation of Korea (NRF) grants funded by the Korean government (MSIT) (2021R1A6A1A10039823 for S. Hong and RS-2023-00272031 for H. Jeon). H. S. Kim acknowledges the National Research Foundation of Korea (NRF) grant, funded by the Korean government (MSIT) (NRF-2022R1A6A1A03051158).

References

1 W. M. Cheng and R. Shang, *ACS Catal.*, 2020, **10**, 9170–9196.
2 X. Lang, X. Chen and J. Zhao, *Chem. Soc. Rev.*, 2014, **43**, 473–486.
3 Y. Yang, S. Niu, D. Han, T. Liu, G. Wang and Y. Li, *Adv. Energy Mater.*, 2017, **7**, 1700555.
4 M. Wang, Z. Hou, A. A. Al Kheraif, B. Xing and J. Lin, *Adv. Healthcare Mater.*, 2018, **7**, 1800351.
5 C. B. Ong, L. Y. Ng and A. W. Mohammad, *Renewable Sustainable Energy Rev.*, 2018, **81**, 536–551.
6 D. Tang, G. Lu, Z. Shen, Y. Hu, L. Yao, B. Li, G. Zhao, B. Peng and X. Huang, *J. Energy Chem.*, 2023, **77**, 80–118.
7 P. Shandilya, S. Sambyal, R. Sharma, P. Mandyal and B. Fang, *J. Hazard. Mater.*, 2012, **428**, 128218.
8 C. M. Wu, S. Naseem, M. H. Chou, J. H. Wang and Y. Q. Jian, *Front. Mater.*, 2019, **6**, 49.
9 G. Longobucco, L. Pasti, A. Molinari, N. Marchetti, S. Caramori, V. Cristino, R. Boaretto and C. A. Bignozzi, *Appl. Catal., B*, 2017, **204**, 273–282.
10 C. Zhai, M. Zhu, D. Bin, H. Wang, Y. Du, C. Wang and P. Yang, *ACS Appl. Mater. Interfaces*, 2014, **6**, 17753–17761.
11 S. Sun, G. Li, S. Zhu, W. Meng, L. Xu, J. Jiang, F. Wang and X. Li, *J. Mater. Chem. A*, 2024, **12**, 17463–17470.
12 W. Meng, S. Sun, D. Xie, S. Dai, W. Shao, Q. Zhang, C. Qin, G. Liang and X. Li, *Mol. Catal.*, 2024, **553**, 113768.
13 C. R. Lhermitte, N. Plainpan, P. Canjura, F. Boudoire and K. Sivula, *RSC Adv.*, 2021, **11**, 198–202.
14 H. Jeon, J. H. Park, S. Han, S. H. Ahn, J. Baik, H. Lee, H. S. Ahn and S. Hong, *Appl. Surf. Sci.*, 2021, **567**, 150834.
15 H. Jeon, D. T. Hoang, J. Baik, S. Hong and H. Lee, *Inorg. Chem.*, 2024, **63**, 12370–12376.
16 K. Sato, H. Yamashita and Y. Kojima, *Jpn. J. Appl. Phys.*, 2024, **63**, 04SP76.
17 Y. Li, X. Wei, X. Yan, J. Cai, A. Zhou, M. Yang and K. Liu, *Phys. Chem. Chem. Phys.*, 2016, **18**, 10255–10261.
18 S. H. Cho, J. M. Suh, B. Jeong, T. H. Lee, K. S. Choi, T. H. Eom, S. W. Choi, G. B. Nam, Y. J. Kim and H. W. Jang, *Small*, 2024, **20**, 2309744.
19 Z. Xi, D. P. Erdosy, A. Mendoza-Garcia, P. N. Duchesne, J. Li, M. Muzzio, Q. Li, P. Zhang and S. Sun, *Nano Lett.*, 2017, **17**, 2727–2731.
20 C. A. García-Negrete, T. C. Rojas, B. R. Knappett, D. A. Jefferson, A. E. H. Wheatley and A. Fernándeza, *Nanoscale*, 2014, **6**, 11090.
21 Z. Han, J. Ren, J. Zhou, S. Zhang, Z. Zhang, L. Yang and C. Yin, *Int. J. Hydrogen Energy*, 2020, **45**, 7223–7233.
22 T. Thilagavathi, D. Venugopal, R. Marnadu, J. Chandrasekaran, D. Thangaraju, B. Palanivel, M. S. Hamdy, M. Shkir and H. E. Ali, *J. Phys. Chem. Solids*, 2021, **154**, 110066.
23 B. Liu, D. Cai, Y. Liu, D. Wang, L. Wang, Y. Wang, H. Li, Q. Li and T. Wang, *Sens. Actuators, B*, 2014, **193**, 28–34.
24 C. V. Ramana, S. Utsunomiya, R. C. Ewing, C. M. Julien and U. Becker, *J. Phys. Chem. B*, 2006, **110**, 10430–10435.
25 M. Saleem, J. Iqbal, A. Nawaz, B. Islam and I. Hussain, *Int. J. Appl. Ceram. Technol.*, 2020, **17**, 1918–1929.
26 T. N. Anh, N. T. Hien, D. T. H. Linh, N. T. Hanh, L. T. Do, N. H. N. M. Hoang, D. V. Quang and V. D. Dao, *Inorg. Chem. Commun.*, 2024, **161**, 112100.
27 P. M. Kodam, P. A. Ghadage, D. Y. Nadargi, K. P. Shinde, I. S. Mulla and J. S. Park, *Ceram. Int.*, 2022, **48**, 17923–17933.
28 J. Zhang, H. Liu, Y. Wang and X. Zhao, *J. Phys. Chem. Lett.*, 2018, **9**, 6814–6817.
29 R. J. Bose, N. Illyasukutty, K. S. Tan, R. S. Rawat, M. V. Matham, H. Kohler and V. M. Pillai, *Appl. Surf. Sci.*, 2018, **440**, 320–330.
30 F. Mehmood, J. Iqbal, T. Jan and Q. Mansoor, *J. Alloys Compd.*, 2017, **728**, 1329–1337.
31 C. Xie, W. Chen, S. Du, D. Yan, Y. Zhang, J. Chen, B. Liu and S. Wang, *Nano Energy*, 2020, **71**, 104653.
32 J. Kaur, K. Anand, N. Kohli, A. Kaur and R. C. Singh, *Chem. Phys. Lett.*, 2018, **701**, 115–125.
33 P. Mandyal, R. Sharma, S. Sambyal, N. Islam, A. Priye, M. Kumar, V. Chauhan and P. Shandilya, *J. Water Process Eng.*, 2024, **59**, 105008.
34 S. S. Kalanur, R. Singh and H. Seo, *Appl. Catal., B*, 2021, **295**, 120269.

35 K. Wang, L. Luo, C. Wang and J. Tang, *Chin. J. Catal.*, 2023, **46**, 103–112.
36 Y. Niu, B. Zhao, Y. Liang, L. Liu and J. Dong, *Ind. Eng. Chem. Res.*, 2020, **59**, 7389–7397.
37 S. Fardindoost, F. Rahimi and R. Ghasempour, *Int. J. Hydrogen Energy*, 2010, **35**, 854–860.
38 Y. Zhu, C. Blackman, P. Zhou, S. K. Ayyala, J. A. Covington, Y. Shen, J. Liang, X. Zhong, C. Knapp and Y. Zhou, *J. Alloys Compd.*, 2023, **936**, 167930.
39 B. Li, X. Zhao, X. H. Luo, W. X. Zhang, C. H. Wen, L. Y. Xu, C. Tang, M. F. Luo and J. Chen, *Appl. Surf. Sci.*, 2024, **650**, 159225.
40 E. Gioria, S. Li, A. Mazheika, R. N. d'Alnoncourt, A. Thomas and F. Rosowski, *Angew. Chem., Int. Ed.*, 2023, **62**, e202217888.
41 S. I. Han, M. Kumar, R. Yeasmin, C. Park, G. Jung, H. Kim, A. S. Khan, H. Dang and H. Seo, *Sens. Actuators, B*, 2024, **404**, 135259.
42 X. Liu, J. Han, X. Qiao, H. Cai, Y. Zhao, Z. Zhang, B. Zhai, T. Ni, C. Zhao and Y. Zhu, *ACS Appl. Mater. Interfaces*, 2024, **16**, 22155–22165.
43 X. Wei, X. He, P. Wu, F. Gong, D. Wang, S. Wang, S. Lu, J. Zhang, S. Xiang, T. Kai and P. Ding, *Int. J. Hydrogen Energy*, 2021, **46**, 27974–27996.
44 T. Li, Y. Shen, X. Zhong, S. Zhao, G. Li, B. Cui, D. Wei and K. Wei, *J. Alloys Compd.*, 2020, **818**, 152927.
45 F. Naaz and T. Ahmad, *Langmuir*, 2023, **39**, 9300–9314.
46 M. Fernández-García, A. Martínez-Arias, A. Fuerte and J. C. Conesa, *J. Phys. Chem. B*, 2005, **109**, 6075–6083.
47 S. Yamazoe, Y. Hitomi, T. Shishido and T. Tanaka, *J. Phys. Chem. C*, 2008, **112**, 6869–6879.
48 B. Ravel and M. J. Newville, *J. Synchrotron Radiat.*, 2005, **12**, 537–541.
49 F. Frati, M. O. J. Y. Hunault and F. M. F. de Groot, *Chem. Rev.*, 2020, **120**, 4056–4110.
50 A. Kumar and R. Ananthakrishnan, *ACS Appl. Energy Mater.*, 2022, **5**, 2706–2719.
51 H. Zhang, Z. Feng, Y. Zhu, Y. Wu and T. Wu, *J. Photochem. Photobiol., A*, 2019, **371**, 1–9.
52 F. Neațu, R. S. Marin, M. Florea, N. Petrea, O. D. Pavel and V. I. Pârvulescu, *Appl. Catal., B*, 2016, **180**, 751–757.
53 Y. Su, Z. Han, L. Zhang, W. Wang, M. Duan, X. Li, Y. Zheng, Y. Wang and X. Lei, *Appl. Catal., B*, 2017, **217**, 108–114.
54 H. Liu, K. Tian, J. Ning, Y. Zhong, Z. Zhang and Y. Hu, *ACS Catal.*, 2019, **9**, 1211–1219.
55 B. Lei, W. Cui, P. Chen, L. Chen, J. Li and F. Dong, *ACS Catal.*, 2022, **12**, 9670–9678.
56 B. D. Mukri, U. V. Waghmare and M. S. Hegde, *Chem. Mater.*, 2013, **25**, 3822–3833.
57 R. Iimura, T. Hasegawa and S. Yin, *Inorg. Chem.*, 2022, **61**, 2509–2516.